Diagnosising the sensitivity of grounding line flux to changes in sub-ice shelf melting

Tong Zhang, Stephen Price, Matthew Hoffman, Xylar Asay-Davis

Fluid Dynamics and Solid Mechanics Group, Los Alamos National Laboratory, New Mexico, United States, 87545

Correspondence: Tong Zhang <tzhang@lanl.gov>

ABSTRACT. Motivated by previous work using ice flow models to quantify ice shelf buttressing and its impacts on the flux of ice across the grounding line (e.g., Fürst and others, 2016; Reese and others, 2018), we seek a better physical understanding for how ice dynamics link small ice thickness perturbations, via changes in sub-ice shelf melting, to changes in ice shelf buttressing and ice flux across the grounding line. More specifically, we seek to define one or more ice shelf buttressing "metrics" that are readily calculated from standard ice sheet model outputs and are simultaneously informative for diagnosing the sensitivity of grounding line flux to ice thickness at specific locations on an ice shelf. By studying the ice dynamics for both idealized (MISMIP+) and realistic (Larsen C) ice shelves, we find that the first principle stress at perturbation locations is the best overall metric for linking local changes in ice shelf dynamics with changes in the integrated grounding line flux. Unfortunately, this metric only shows a robust relationship with the integrated grounding line flux for regions near the center of an ice shelf; for points too near the grounding line or too near the calving front, no clear relationship exists between any of the readily calculable metrics explored here and changes in grounding line flux. This motivates our exploration of an adjoint-based method for defining grounding line flux sensitivity to local changes in ice shelf

geometry. Using the same idealized and realistic test cases, we demonstrate that this method is equivalent to the sensitivity analysis of (Reese and others, 2018) but requires only a single model adjoint solve. Thus we suggest that the adjoint-based method can provide a model run-time means of analyzing grounding line flux sensitivity to changes in sub-ice shelf melting.

INTRODUCTION

Marine ice sheets like West Antarctica (and to a lesser extent, portions of East Antarctica) are grounded below sea level and their bedrock would remain so even after full isostatic rebound (Barletta and others, 2018). This and the fact that ice sheets generally thicken inland lead to a geometric configuration that is unstable; a small increase in flux at the grounding line thins the ice there, leading to floatation, a retreat of the grounding line into deeper water, further increases in flux (due to thicker ice), and further thinning and grounding line retreat. This theoretical "marine ice sheet instability" mechanism (Mercer, 1978; Schoof, 2007) is supported by idealized (Schoof, 2012; Asay-Davis and others, 2016) and realistic ice sheet modeling (Royston and Gudmundsson, 2016) experiments and some studies (Joughin and others, 2014; Rignot and others, 2014) argue that such an instability is currently under way along outlet glaciers of Antarctica's Amundsen Sea Embayment (ASE). The relevant perturbation for grounding line retreat in the ASE is thought to be intrusions of relatively warm, intermediate depth ocean waters onto the continental shelves [ref to recent review papers in Oceanography? or other recent reviews? **TZ: perhaps Xylar can help with this?**], which have reduced the thickness and extent of marginal ice shelves via increased submarine melting [REFS]. These reductions are critical because fringing ice shelves restrict the flux of ice across their grounding lines farther upstream – the so-called "buttressing" affect of ice shelves (Gudmundsson and others, 2012; Gudmundsson, 2013; De Rydt and others, 2015) – which makes them a critical control on ice flux from Antarctica to the ocean.

On ice shelves, gradients in hydrostatic pressure are balanced by the primarily extensional flow of ice towards the calving front (Mutter, 1983; Morland, 1987; Schoof, 2007) and, in theory, a one horizontal dimension (x-z) ice shelf provides no buttressing (Schoof, 2007; Gudmundsson, 2013). (*SP: I wonder if this requires a monotonic decrease in ice shelf thickness though?* **TZ: I think so**) For realistic, three-dimensional ice shelves however, buttressing results from three main sources: 1) compressive ice flow 2) lateral shear, and 3) "hoop" stress (Pegler and Worster, 2012). Both compressive and lateral shear stresses supply backward resistences to extentional ice shelf flow, and the "hoop" stress is a transverse stress arising from azimuthal extension existing in the diverging ice flow regions (Wearing, 2016). (*For completeness, we should probably briefly describe how each of these contributes to buttressing rather than assume people already know (?). The first two are easy. I'm not sure about the 3rd.* **TZ: I add a sentence in the previous line**) Due to the complex geometries, kinematics, and dynamics of real ice shelves, an understanding of the specific processes and locations that control ice shelf buttressing is far from straigtforward.

Several recent studies apply whole-Antarctic ice sheet models optimized to present-day observations towards improving our understanding for how Antarctica ice shelves limit flux across the grounding line and, by extension, ice dynamics farther inland. Fürst and others (2016) calculated the buttressing across Antarctica ice shelves along two major directions (flow and second principle stress) and evaluated their impacts on upstream ice dynamics to identify regions of the ice shelves that are dynamically "passive", such that increased submarine melting, or even complete removal of ice in these areas should not significantly alter local or regional ice dynamics or the flux of ice upstream. Reese and others (2018) used perturbation experiments to link small, localized decreases in ice shelf thickness to changes in integrated grounding line flux (GLF), thereby providing a map of GLF sensitivity to local increases in submarine melt rates.

Motivated by these studies, we build on and extend the methods and analysis of Fürst and others (2016) and Reese and others (2018) in order to make progress towards answering the following questions: (1) How do local and regional changes in ice shelf geometry affect distal changes in GLF? (2) Can local or regional ice shelf dynamics explain GLF sensitivity to local or regional changes in ice shelf thickness? (3) Can we derive and define new tools and analyses for understanding how observed or modeled spatial patterns in submarine melting influence GLF and, by extension, project how changes in submarine melt pattern and magnitude will impact GLF in the future?

Below, we first provide a brief description of the ice sheet model used in our study. We follow with a description of the model experiments and a discussion of the experimental results and their interpretation. We then demonstrate and discuss the pros and cons of a number of possible metrics for quantifying GLF sensitivity to changes in submarine melt. Based on limitations in all metrics explored here, we conclude by proposing and demonstrating an adjoint-based calculation that provides a sensitivity map analogous to that from the Reese and others (2018) perturbation experiments but at the cost of a single model adjoint solve. (**TZ: we should revisit this paragraph at some point after we finish most of revisions in the manuscript**)

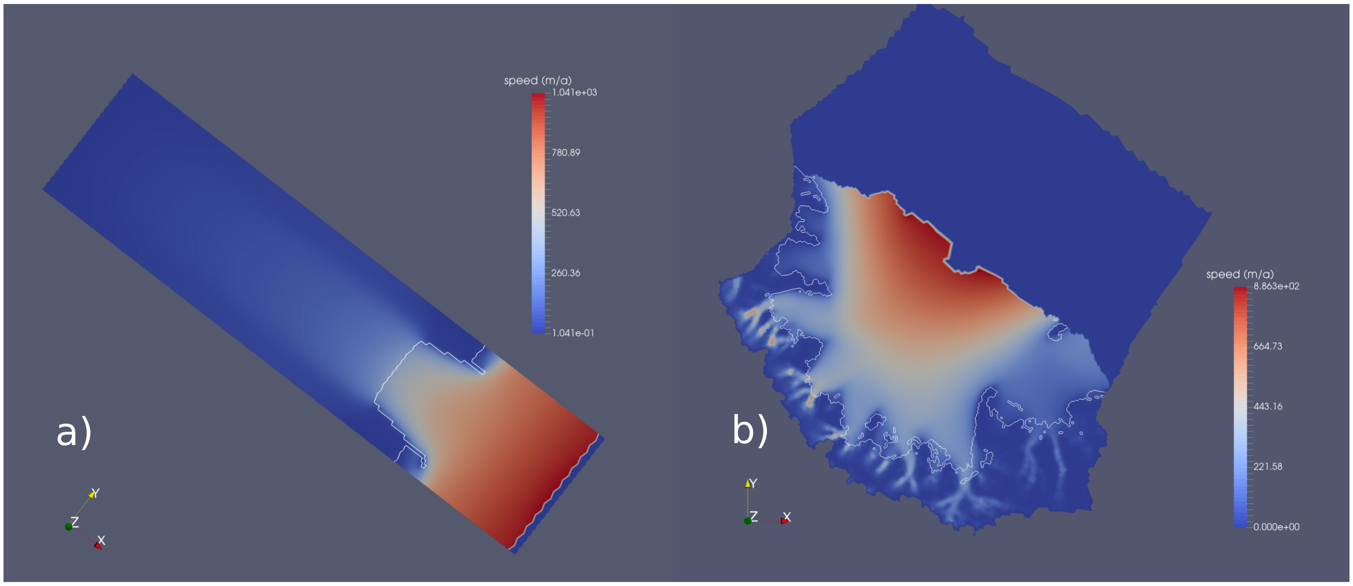

Fig. 1. Plan view of steady-state surface ice speeds for MISMIP+ (a) and present-day surface ice speed for Larsen C ice shelf (b). The white curves show the grounding lines.

MODEL DESCRIPTION

SP: I built out this section a bit more. We can reduce later on if needed but it seemed a bit too thin. Note that this is mostly copied and lightly edited from the MALI paper, so we'll have to look over carefully and make sure it doesn't end up looking self-plagiarized. We use the MPAS-Albany Land Ice model (MALI; Hoffman and others (2018)), which solves the three-dimensional, first-order approximation to the Stokes momentum balance for ice flow[1]. Using the notation of Perego and others (2012) and Tezaur and others (2015a) this can be expressed as,

$$\begin{cases} -\nabla \cdot (2\mu_e \dot{\boldsymbol{\epsilon}}_1) + \rho_i g \frac{\partial s}{\partial x} & = & 0, \\ -\nabla \cdot (2\mu_e \dot{\boldsymbol{\epsilon}}_2) + \rho_i g \frac{\partial s}{\partial y} & = & 0, \end{cases} \tag{1}$$

where x and y are the horizontal coordinate vectors in a Cartesian reference frame, $s(x, y)$ is the ice surface elevation, ρ_i represents the ice density, g the acceleration due to gravity, and $\dot{\boldsymbol{\epsilon}}_{1,2}$ are the two dimensional strain rate vectors given by

$$\dot{\boldsymbol{\epsilon}}_1 = \begin{pmatrix} 2\dot{\epsilon}_{xx} + \dot{\epsilon}_{yy}, & \dot{\epsilon}_{xy}, & \dot{\epsilon}_{xz} \end{pmatrix}^T, \tag{2}$$

[1]See Schoof and Hewitt (2013) for for a full description of the Stokes momentum balance for ice flow and its lower-order approximations.

and

$$\dot{\boldsymbol{\epsilon}}_2 = \begin{pmatrix} \dot{\epsilon}_{xy}, & \dot{\epsilon}_{xx} + 2\dot{\epsilon}_{yy}, & \dot{\epsilon}_{yz} \end{pmatrix}^T. \tag{3}$$

The "effective" ice viscosity, μ_e in Equation 1, is given by

$$\mu_e = \gamma A^{-\frac{1}{n}} \dot{\epsilon}_e^{\frac{1-n}{n}}, \tag{4}$$

where γ is an ice stiffness factor, A is a temperature-dependent rate factor, $n = 3$ is the power-law exponent, and the effective strain rate, $\dot{\epsilon}_e$, is defined as

$$\dot{\epsilon}_e \equiv \left(\dot{\epsilon}_{xx}^2 + \dot{\epsilon}_{yy}^2 + \dot{\epsilon}_{xx}\dot{\epsilon}_{yy} + \dot{\epsilon}_{xy}^2 + \dot{\epsilon}_{xz}^2 + \dot{\epsilon}_{yz}^2\right)^{\frac{1}{2}}. \tag{5}$$

Gradients in the horizontal velocity components, u and v, contribute to the individual strain rate terms in Equation 5 and are given by

$$\dot{\epsilon}_{xx} = \frac{\partial u}{\partial x}, \quad \dot{\epsilon}_{yy} = \frac{\partial v}{\partial y}, \quad \dot{\epsilon}_{xy} = \frac{1}{2}\left(\frac{\partial u}{\partial y} + \frac{\partial v}{\partial x}\right), \quad \dot{\epsilon}_{xz} = \frac{1}{2}\frac{\partial u}{\partial z}, \text{ and } \dot{\epsilon}_{yz} = \frac{1}{2}\frac{\partial v}{\partial z}. \tag{6}$$

A stress free upper surface is enforced through

$$\dot{\boldsymbol{\epsilon}}_1 \cdot \mathbf{n} = \dot{\boldsymbol{\epsilon}}_2 \cdot \mathbf{n} = 0, \tag{7}$$

where $\mathbf{n}$ is the outward pointing normal vector at the ice sheet upper surface, $z = s(x, y)$. The lower surface is allowed to slide according to the continuity of basal tractions,

$$2\mu_e \dot{\boldsymbol{\epsilon}}_1 \cdot \mathbf{n} + \beta u = 0, \;\; 2\mu \dot{\boldsymbol{\epsilon}}_2 \cdot \mathbf{n} + \beta v = 0, \tag{8}$$

where β is a spatially variable, linear-friction coefficient. On lateral boundaries in contact with the ocean, the portion of the boundary above sea level is stress free while the portion below sea level feels the ocean hydrostatic pressure according to

$$2\mu_e \left(\dot{\boldsymbol{\epsilon}}_1 \cdot \mathbf{n}, \, \dot{\boldsymbol{\epsilon}}_2 \cdot \mathbf{n}, \, 0\right)^T - \rho_i g(s - z)\mathbf{n} = \rho_o g \max(z, 0)\mathbf{n}, \tag{9}$$

where ρ_o represents the density of ocean water and $\mathbf{n}$ the outward pointing normal vector to the lateral boundary (i.e., parallel to the (x, y) plane).

A more complete description of the full MALI model, including the implementations for mass and energy conservation, can be found in Hoffman and others (2018). Additional details about the Albany momentum balance solver can be found in Tezaur and others (2015a,b).

Here, we apply MALI to experiments on both idealized and realistic marine-ice sheet geometries. For our idealized domain and model state, we start from the equilibrium initial conditions for the MISMIP+ experiments, as described in Asay-Davis and others (2016) and Cornford and others (MISMIP+ papers) (**TZ: is it the same paper as Xylar's?**). The model mesh is spatially uniform at 2 km resolution. For our realistic domain, we use Antarctica's Larsen C ice shelf and its upstream catchement area. The model state is based on the optimization of the ice stiffness (γ in Equation 4) and basal friction (β in Equation 8) coefficients to match present-day velocities (Rignot and others, 2014) using adjoint-based methods discussed in Perego and others (2014) and Hoffman and others (2018). The domain geometry is based on BEDMAP2 (Fretwell and others, 2013) and ice temperatures, which are held fixed for this study, are based on Liefferinge and Pattyn (2013). Mesh resolution coarsens to 20 km in the ice sheet interior and is no greater than 6 km within the ice shelf *This seems coarse to me ... don't we go to finer resolution, e.g. 2 km, near the g.l.?* **TZ: I think it means the other way around – the res. is not coarser than 6 km in ice shelf (i.e., >2 km and < 6 km)**. Following optimization to present-day velocities, the model is relaxed using a 100 year forward run and it is this initial condition from which the experiments discussed below are conducted. Both the MISMIP+ and Larsen C experiments use 10 vertical layers that are finest near the bed and coarsen towards the surface (4% and 23% of the total thickness, respectively). The grounding line position is determined from hydrostatic equilibrium and a sub-element parameterization analogous to method SEP3 from Seroussi and others (2014) is used to define basal friction coefficient values at the grounding line.

PERTURBATION EXPERIMENTS

To explore the sensitivity of changes in GLF to small changes in ice shelf thickness, we conduct a number of perturbation experiments analagous to those of Reese and others (2018). Using diagnostic model solutions, we first study the instantaneous response of GLF for the idealized geometry and initial state provided by the MISMIP+ experiment (Asay-Davis and others, 2016). We then conduct a similar study but using a realistic configuration and initial state for Antarctica's Larsen C ice shelf.

Our experiments are conducted in a manner similar to those of Reese and others (2018). We perturb the coupled ice sheet-shelf system by decreasing the ice thickness uniformly by 1 m over square grid "boxes" covering the base of the ice shelves, after which we examine the instantaneous impact on kinematics and dynamics (discussed further below). For MISMIP+, the uniform, 2 km mesh implies that grid cell centers naturally align with these boxes. For the Larsen C ice shelf, horizontal mesh resolution is spatially variable and we assign each grid cell to fall within one and only one box based on its location. For MISMIP+, we use 2×2 km square boxes that are also the real cell size. For Larsen C, we only use 20×20 km square boxes (i.e., as in Reese and others (2018)). Lastly, for the MISMIP+ 2 km experiments we note that, in order to save on computing costs, we only perturb the region of the ice shelf for which $x < 530$ km (the area over which the ice shelf is likely lateraly buttressed) and $y > 40$ km (one half of the ice shelf due to the symmetry about the centerline).

Similar to Reese and others (2018), we define a GLF response number

$$N_r = \left(\frac{R}{P}\right)^k, \tag{10}$$

where R is the ice flux change integrated along the entire grounding line, P is the mass associated with a single grid box perturbation (e.g.,2 km×2 km ×0.001 km for the MISMIP+ perturbation experiments) and k is a power-law index that allows for the possiblity of a nonlinear relationship between ice shelf buttressing and the change in GLF (see also Schoof (2007)). Here, we use $k = 1/n$ ($n = 3$).

Despite the existence of many different factors (ice flow directions, horizontal gradients of ice shelf geometry, stress fields, strain-rate fields, perturbation locations, etc), we here mainly present the results of the stress fields and the distances between perturbations and GL, as they appears to correlate more closely to the sensitivity of GL flux change to ice shelf perturbations. Similar to Fürst and others (2016) (Eqn 11), we calculate buttressing numbers (N_b) as follows,

$$N_b = 1 - \frac{\sigma_{nn}}{N_0}, \tag{11}$$

where N_0 is the vertically integrated ocean pressure ($N_0 = 0.5\,(1 - \rho_i/\rho_w)\,gH$). ρ_i (910 kg m^3) and ρ_w (1028 kg m^3) are the density of ice and ocean water, respectively. σ_{nn} is the normal stress along certain horizontal direction.

RESULTS AND DISCUSSIONS

Linear relationship between buttressing (N_b) and GL flux responses (N_r)

The decrease of ice shelf buttressing tends to induce the increase of GLF (Gagliardini and others, 2010). Therefore, the highly buttressed regions are in general more sensitive to sub-ice shelf melting for marine ice sheet dynamics. It is thus useful to understand more quantitatively the relationship between the buttressing "strength" (number) and the GLF changes. Can we predict the changes of GLF simply by the buttressing

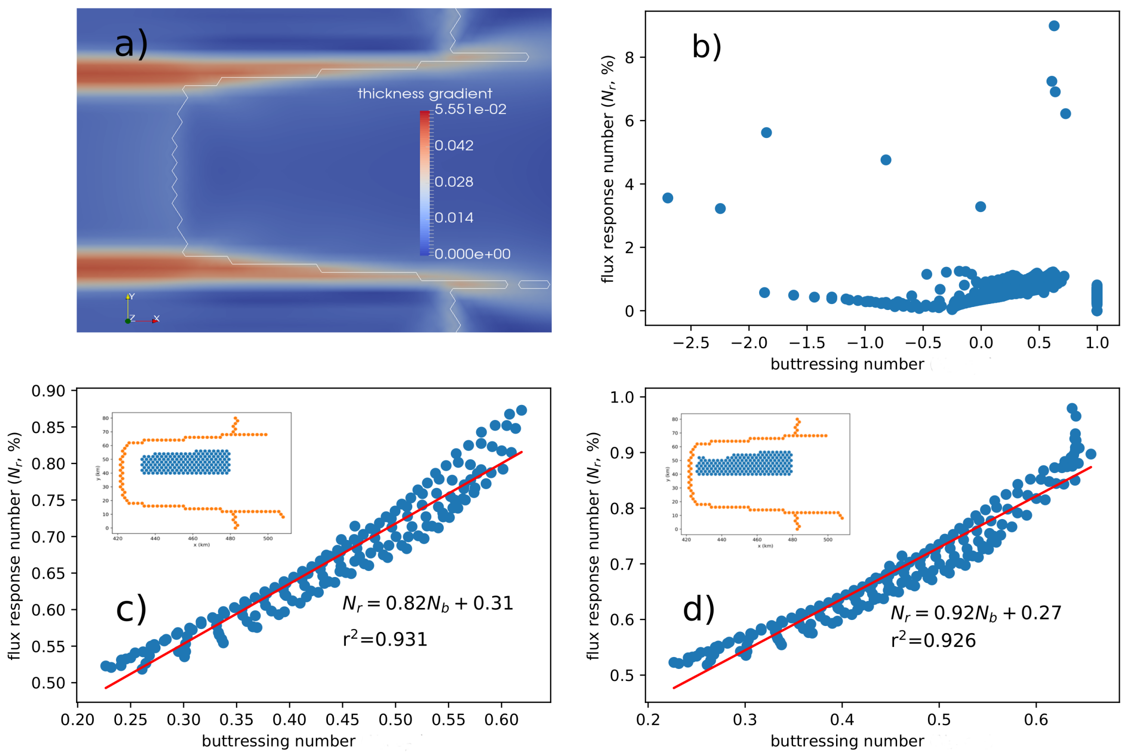

Fig. 2. (a) The magnitude of ice thickness gradient around GL (white curve) for the steady-state MISMIP+ geometry; (b) The relationship of N_b-N_r for all perturbation points; (c) The relationship of N_b-N_r for perturbation points that are >10 km away from GL; (d) The relationship of N_b-N_r for perturbation points with thickness gradient $<7times10^{-3}$. The red (blue) dots in the insets are GL (perturbation) cells.

number (N_b)? By calculating the buttressing number (N_b) along the first principle stress (σ_{p1}) direction, we can see very weak N_b-N_r correlations from the results of all perturbation experiments (Fig 2b). However, if we do not consider the perturbation points that are weakly buttressed ($x > 480$ km; near the open shelf region) and are close to GL (the minimum distances between GL and perturbation points are greater than 5 km), we can clearly see a strong linear N_b-N_r regression (Fig 2c). A similar strong linearity can also be found if we apply a different filtering approach using the ice thickness gradient field (Fig 2a), i.e., we keep the perturbation points that have thickness gradients smaller than 0.0007 (Fig 2d). This nonlinearity feature is likely caused by the intensive shearing and complex ice flow mechanics near GL (a strong transition zone from relatively slow grounded ice flow to fast extensively floating ice flow). We can again see this non-linearity region in our adjoint sensitivity experiments (Fig. 9 in section "Adjoint sensitivity").

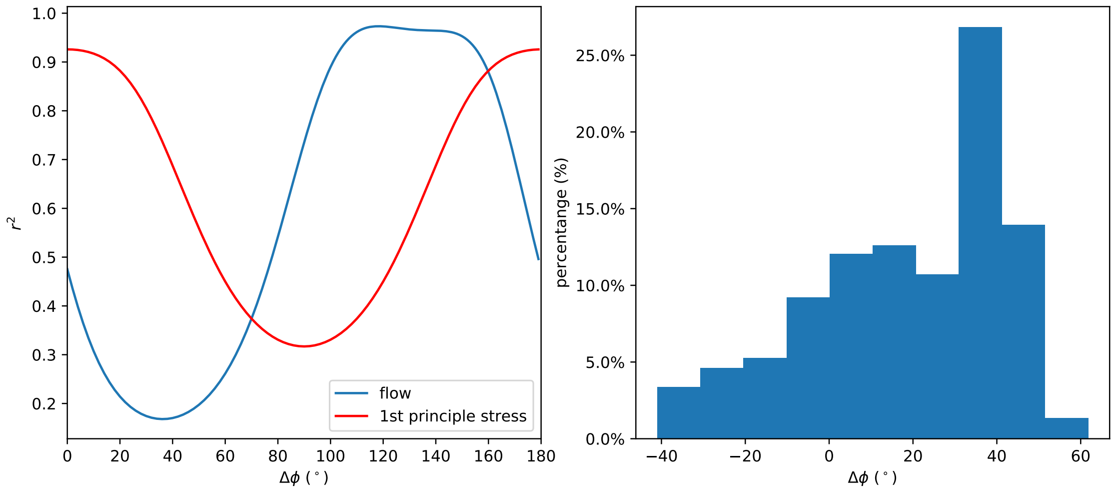

Fig. 3. (a) The N_b-N_r regression coefficients for each direction rotated anti-clock-wisely from the σ_{p1} (red) and flow direction (blue); (b) The histogram of the angle differences between flow and σ_{p1} directions. The perturbation points we apply here are the same as in Figure 2d.

The buttressing directions

According to Equation 11, the buttressing number N_b is computed by the normal stress (σ_{nn}) along specific directions. Therefore, the buttressing at certain perturbation points can be various for different directions we apply. In Fürst and others (2016) the buttressing along two significant directions (flow and second principle stress (σ_{p2})) was analyzed, and found that the σ_{p2} buttressing, which points to the most compression direction, has the maximum impacts on the "passive" ice shelf regions. Here we get the correlation numbers (r^2) between N_r and N_b for different directions with respect to the first principle stress and flow direction, respectively (Fig 3). Differently, we find that N_b along the σ_{p1} direction shows the best regression performance, whereas the σ_{p2} appears to show the weakest correlations to N_r. This can be further testified by looking at the angle differences between σ_{p1} and flow directions ($\Delta\phi = \phi_{flow} - \phi_{\sigma_{p1}}$). From Figure 3b, we see that for around 50% of the perturbation points, their flow directions are around 30–50 degree more than the σ_{p1} directions, which is consistent with the phase differences in Figure 3a. If we add around 40 degree on top of the flow direction (blue curve), the new direction will be likely aligned closely with the σ_{p2} direction, which is consequently pointing to the smallest r^2 number for the σ_{p1} (red) curve. This indicates that the local maximum buttressing relating to σ_{p2} is unnecessarily corresponding to the integrated instantaneous GLF responses.

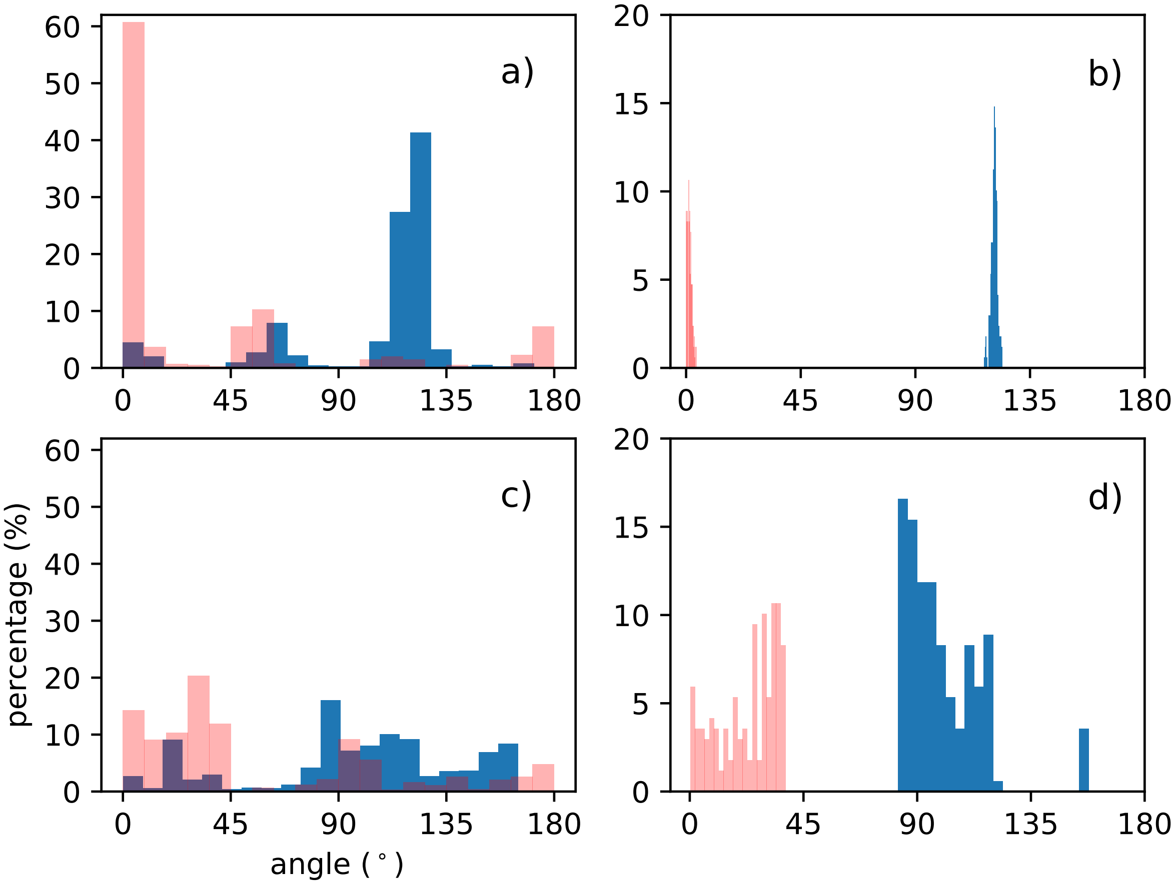

Fig. 4. Histograms of the frequency of the neighboring maximum (red) and minimum (blue) velocity change around all perturbation points (a and c) and around the same selected perturbation points (b and d) as Figure 2d (**TZ: this figure still needs double check!**)

Possible controlling factors

Further clues of the impacts from different chosen directions can be found in Figure 4. We analyzed the number of maximum (light red) and minimum (blue) velocity changes around each perturbation point for the cases using flow (Fig 4a) and σ_{p1} directions (Fig 4b). Figure 4a and c contain all perturbation points while Figures 4b and d only include the filtered perturbation points as in Figure 2d. For the flow direction results, most of the maximum (minimum) velocity change events occur along the flow (120 degree) direction. The σ_{p1} direction results are more spread than of the flow direction results. However, it is still clear that most of the maximum (minimum) velocity change events are aligned near the first (second) principle stress direction, a supporting evidence for our previous findings.

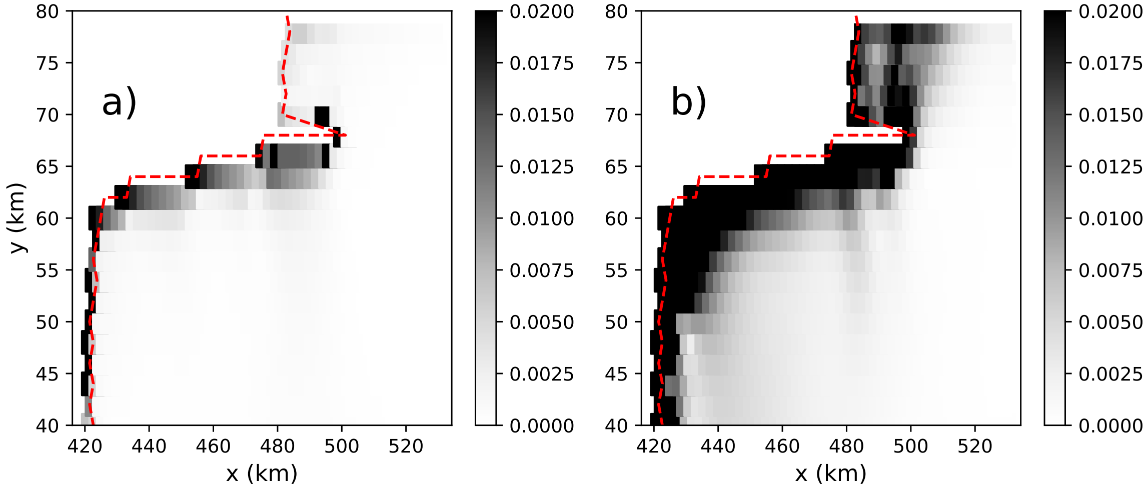

Fig. 5. The standard deviations of Ψ along GL for each perturbation point for the case of σ_{p1} (a) and σ_{p2} (b).

Another evidence is the standard deviation of the differences between the relative changes of stress and velocity (Ψ) along GL (Fig 5).

$$\Psi = \frac{\sigma_p - \sigma_c}{\sigma_c} - \frac{u_p - u_c}{u_c}, \tag{12}$$

where the subscripts p and c denote perturbation experiments and ctrl runs. σ and u denote the stress component and ice velocity, respectively. This is a measure of the consistency of velocity and stress variances along GL under certain perturbation experiments. Here we choose σ_{p1} and σ_{p2} for instances, i.e., we set σ in Equation 12 to σ_{p1} and σ_{p2}. Overall, the σ_{p1} case (Fig 5a) shows smaller standard deviations, especially for perturbation points close to GL, than the σ_{p2} case (Fig 5b). This possibly indicates that GLF are more relevant to the changes of σ_{p1} along GL, compared to the σ_{p2} case, which can be clearly found if we look at some specific perturbation example as shown in Figure 6.

One of the possible reasons for us seeing such direction-dependent correlations might be due to the perturbation propagation features on ice shelves. The energy of perturbation propagates with the group velocity if we decompose it using Fourier transform. A similar example can be found in (Gudmundsson, 2003). Using very simplified geometry Gudmundsson (2003) analyzed the propagation of basal perturbation to glacier surface and found that the direction of group velocity is aligned closely with the main flow. The existence of preferred propagation direction for the perturbations can possibly lead to our findings that favor the first principle stresses (**TZ: I am still not able to explain why it's exactly the first principle stress direction :(**).

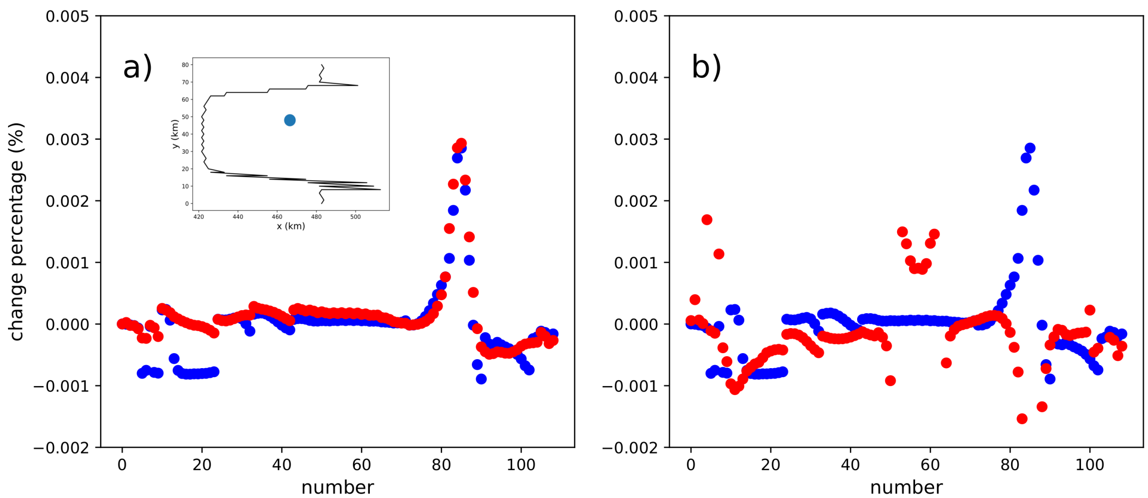

Fig. 6. An example showing the relationship of the change of velocity (blue) with σ_{p1} (red; a) and σ_{p2} (red; b). The x-axis shows the cell number along GL. The inset shows the perturbation location.

Application on Larsen C ice shelf

To validate if there are the same N_b-N_r patterns as in the MISMIP+ case for realistic ice shelves, we apply the same analysis processes as above to the Larsen C ice shelf. Because the mesh resolution varies from GL to calving front, we apply 20 km $\times$ 20 km square boxes to the perturbation experiments and adjust the box areas by counting actual cell numbers that each box includes. In addition, to account for the complex geometry (GL shape and ice rises) of Larsen C ice shelf, we use two different perturbation sets with and without including near-GL boxes for investigating further the nonlinearity feature we observe in the above MISMIP+ section.

From Figure 7a, we can see similar N_b-N_r correlation patterns to that of the MISMIP+ case. Along the σ_{p1} direction we have the best N_b-N_r correlations ($\Delta\phi = 0$, red curve), whereas along the σ_{p2} ($\Delta\phi = 90$, red curve) direction they are the most insignificant. The phase difference between the σ_{p1} and flow direction results can also be partially explained by their respective angle differences. In Figure 7b we can find the angles of flow directions are mostly around 90–100 degrees larger than that of the σ_{p1} directions. This is a bit biased than the around 70 degree difference in Figure 7a. However, considering the stress values (and thus N_b) for each perturbation box are averaged over multiple cells, we argue this difference is probably an acceptable error during our calculation.

By including some near-GL perturbation boxes (Fig. 7c and d), the r^2 features get disturbed as well. Although the angle differences between the flow and σ_{p1} directions are still mostly near 90 degree, there

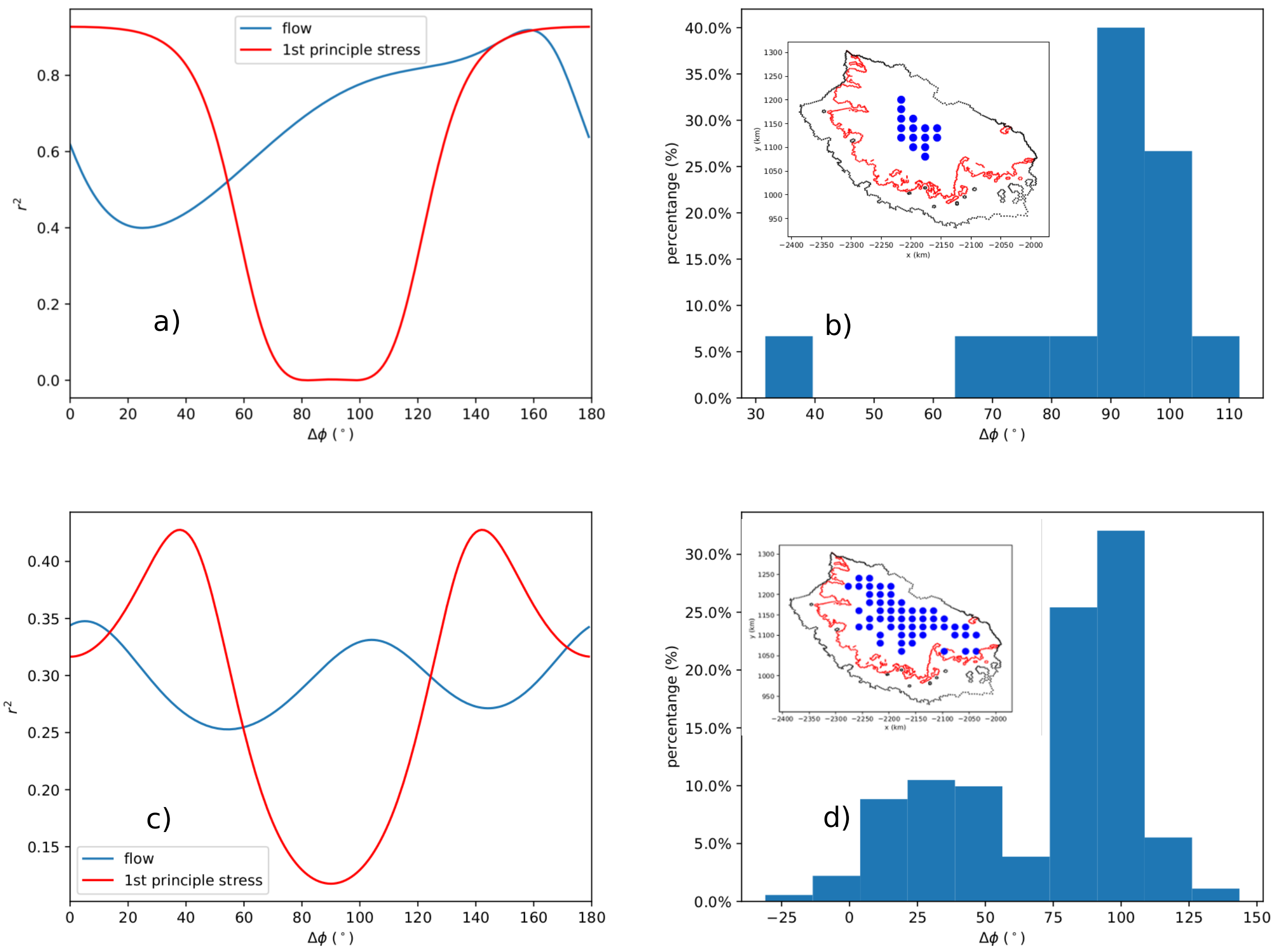

Fig. 7. (a, c) The N_b-N_r regression coefficients for each direction rotated anti-clock-wisely from the σ_{p1} (red) and flow direction (blue); (b, d) The histogram of the angle differences between flow and σ_{p1} directions. The insets in b) and d) show the perturbation boxes (blue circles).

are no longer clear patterns in the phase differences for the corresponding r^2 curves. In addition, the σ_{p1} directions are also no longer indicating the best r^2 correlations. However, the directions along σ_{p2} appears to still pointing to the weakest N_b-N_r correlations, despite the overall much smaller r^2 values in this case.

Impacts of near-GL perturbations

For the near-GL perturbations, it is hard to find similar linear regression relationship as discussed above. Alternatively, they are largely controlled by the distance between GL and perturbation points and also by the geometric features around them. As the perturbation decays over distance (Lick, 1970), the neighboring GL cells of those near-GL perturbations will relatively easily detect the perturbation energy. This can be verified by looking at the standard deviations of GL velocity change due to each perturbation (Fig 8). For

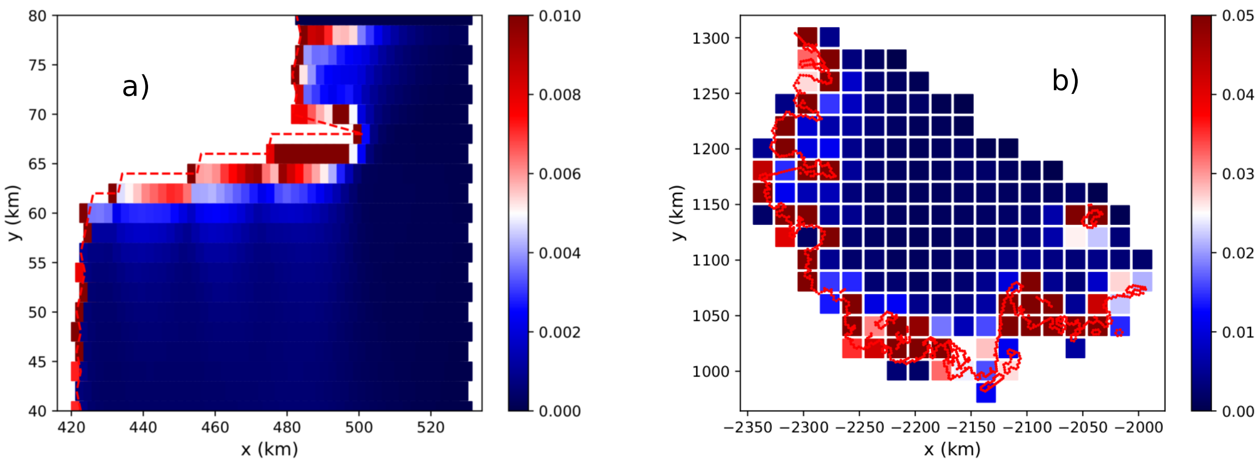

Fig. 8. Standard deviation of velocity change along GL for each perturbation point for the MISMIP+ (a) and Larsen C (b) experiment. The red dashed lines (points) are the GLs for MISMIP+ (a) and Larsen C (b) .

perturbations close to GL, their corresponding GL flux changes are in general confined to local regions, while in the remote GL sections the velocity changes are often negligible, resulting in large standard deviations. This can possibly cause spatial heterogeneity of GL retreating if the sub-shelf melting is very close to GL and is heavily local confined.

The propagation of perturbation can also be impacted by the spatial GL geometry, e.g., they can be blocked by the local GL. For example, the perturbation at around x = 480 km and y = 65 km in Figure 8a can not directly impact the ice flow on the other side of the grounded peninsula (e.g., x=485 km, y=70km) in the same way as for it's neighboring cells. This is one of the major factors that complicate our diagnostic analysis for real ice shelves (for example, Larsen C) containing complex GL shapes and geometries.

Adjoint sensitivity

Need helps from Steve and Mauro!

CONCLUSIONS

From this study we find that the sensitivity of grounding line (GL) flux to melt perturbations beneath ice shelves appears to be linearly related to the buttressing number for certain stress field of the ice flow regime when the perturbations are located near the center of ice shelves. We can divide an ice shelf into three different geometric regions: 1) near GL where the shear margins dominate; 2) near the calving fronts where ice can be considered as "passive" and 3) the central regions of ice shelf. Though it is ambiguous to

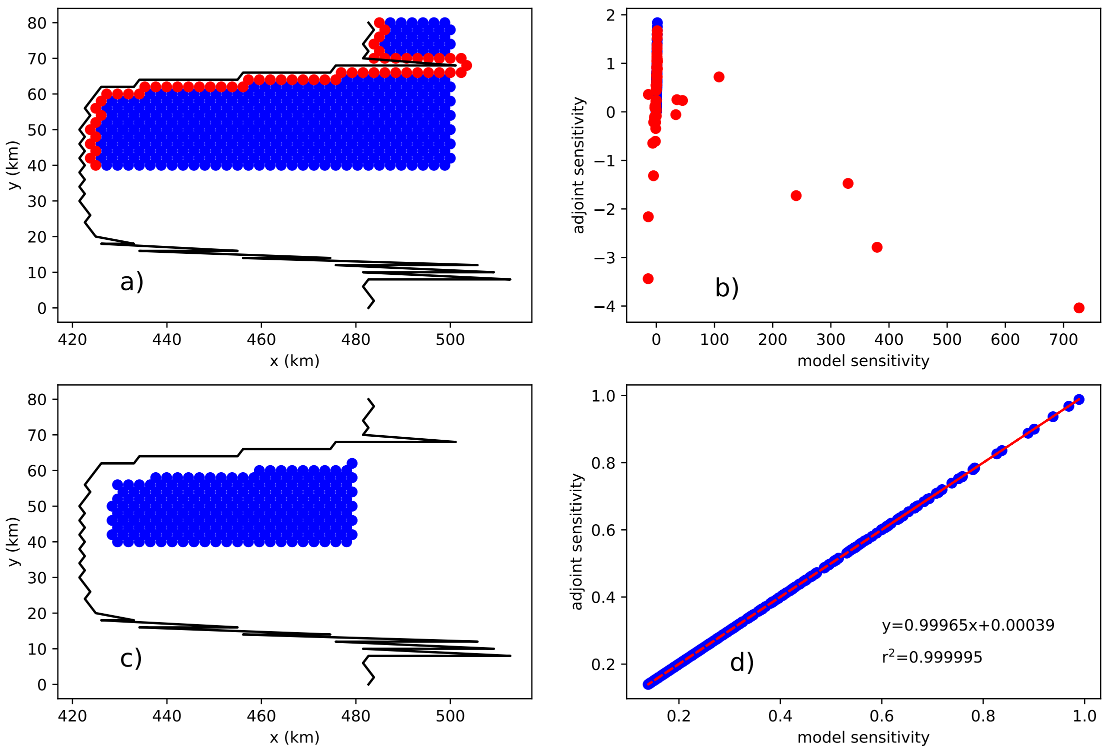

Fig. 9. (a, c) Perturbation points. The red points indicate near-GL (<2 km) points. GL is the black curve; (b, d) Model sensitivity by perturbation experiments versus adjoint sensitivity. The red dashed curve shows their linear regression.

indentify the boundaries of those three sub-regions, we find that both the shear margins and passive ice regions show very weak linear connections to GL flux changes. The shear margins are strongly impacted by the upstream grounded stream flows and the passive ice shelf basically has negligible contribution to GL dynamics.

The buttressing of ice shelf resists ice flows from upstream. The maximum buttressing number (calculated from the second principle stress σ_{p2}) is a commonly used metric to quantify the buttressing effects of ice shelf, doesn't show clear correlations to the changes of GL flux. Among many possible factors we find that the distance away from perturbation locations may be a critical control for perturbation propagation across ice shelves, which is important for understanding the relationships between the stress field of the ice shelf and the GL flux changes. The GL ice speed changes may be more correlated to the changes of the first principle stress (σ_{p1}) and normal stress along flow (σ_f) than other stress components, for example, the second principle stress (σ_{p2}) and the shear stress (σ_s), indicating that the stress component (σ_{p2}) that contribute significantly to buttressing is not necessarily related to the progapation of buttressing.

The linear N_b-N_r relationships presented in this study are based on small (1 m) thickness perturbations. However, it's still unclear if they can stand for large melts at the bottom of ice shelves (**Perhaps we also need to do large perturbation experiments?**). Despite the progress we have made in this study, we suggest to apply a fully-developed perturbation propagation model for further understanding the physics of GL flux changes under ocean forcings.

ACKNOWLEDGEMENT

REFERENCES

Asay-Davis XS, Cornford SL, Durand G, Galton-Fenzi BK, Gladstone RM, Gudmundsson H, Hattermann T, Holland DM, Holland D, Holland PR and others (2016) Experimental design for three interrelated marine ice sheet and ocean model intercomparison projects: Mismip v. 3 (mismip+), isomip v. 2 (isomip+) and misomip v. 1 (misomip1). *Geoscientific Model Development*, **9**(7), 2471–2497

Barletta VR, Bevis M, Smith BE, Wilson T, Brown A, Bordoni A, Willis M, Khan SA, Rovira-Navarro M, Dalziel I and others (2018) Observed rapid bedrock uplift in amundsen sea embayment promotes ice-sheet stability. *Science*, **360**(6395), 1335–1339

De Rydt J, Gudmundsson G, Rott H and Bamber J (2015) Modeling the instantaneous response of glaciers after the collapse of the larsen b ice shelf. *Geophysical Research Letters*, **42**(13), 5355–5363

Fretwell P, Pritchard HD, Vaughan DG, Bamber J, Barrand N, Bell R, Bianchi C, Bingham R, Blankenship D, Casassa G and others (2013) Bedmap2: improved ice bed, surface and thickness datasets for antarctica

Fürst JJ, Durand G, Gillet-Chaulet F, Tavard L, Rankl M, Braun M and Gagliardini O (2016) The safety band of antarctic ice shelves. *Nature Climate Change*, **6**(5), 479

Gagliardini O, Durand G, Zwinger T, Hindmarsh R and Le Meur E (2010) Coupling of ice-shelf melting and buttressing is a key process in ice-sheets dynamics. *Geophysical Research Letters*, **37**(14)

Gudmundsson G (2013) Ice-shelf buttressing and the stability of marine ice sheets. *The Cryosphere*, **7**(2), 647–655

Gudmundsson GH (2003) Transmission of basal variability to a glacier surface. *Journal of Geophysical Research: Solid Earth*, **108**(B5)

Gudmundsson H, Krug J, Durand G, Favier L and Gagliardini O (2012) The stability of grounding lines on retrograde slopes. *The Cryosphere*, **6**(6), 1497–1505

Hoffman MJ, Perego M, Price SF, Lipscomb WH, Zhang T, Jacobsen D, Tezaur I, Salinger AG, Tuminaro R and Bertagna L (2018) Mpas-albany land ice (mali): a variable-resolution ice sheet model for earth system modeling using voronoi grids. *Geoscientific Model Development*, **11**(9), 3747–3780 (doi: 10.5194/gmd-11-3747-2018)

Joughin I, Smith BE and Medley B (2014) Marine ice sheet collapse potentially under way for the thwaites glacier basin, west antarctica. *Science*, **344**(6185), 735–738

Lick W (1970) The propagation of disturbances on glaciers. *Journal of Geophysical Research*, **75**(12), 2189–2197

Liefferinge BV and Pattyn F (2013) Using ice-flow models to evaluate potential sites of million year-old ice in antarctica. *Climate of the Past*, **9**(5), 2335–2345

Mercer JH (1978) West antarctic ice sheet and co2 greenhouse effect: a threat of disaster. *Nature*, **271**(5643), 321

Morland L (1987) Unconfined ice-shelf flow. In *Dynamics of the West Antarctic Ice Sheet*, 99–116, Springer

Mutter K (1983) *Theoretical glaciology*

Pegler SS and Worster MG (2012) Dynamics of a viscous layer flowing radially over an inviscid ocean. *Journal of Fluid Mechanics*, **696**, 152–174

Perego M, Gunzburger M and Burkardt J (2012) Parallel finite-element implementation for higher-order ice-sheet models. *Journal of Glaciology*, **58**(207), 76–88, ISSN 00221430 (doi: 10.3189/2012JoG11J063)

Perego M, Price S and Stadler G (2014) Optimal initial conditions for coupling ice sheet models to earth system models. *Journal of Geophysical Research: Earth Surface*, **119**(9), 1894–1917

Reese R, Gudmundsson GH, Levermann A and Winkelmann R (2018) The far reach of ice-shelf thinning in antarctica. *Nature Climate Change*, **8**(1), 53

Rignot E, Mouginot J, Morlighem M, Seroussi H and Scheuchl B (2014) Widespread, rapid grounding line retreat of pine island, thwaites, smith, and kohler glaciers, west antarctica, from 1992 to 2011. *Geophysical Research Letters*, **41**(10), 3502–3509

Royston S and Gudmundsson GH (2016) Changes in ice-shelf buttressing following the collapse of larsen a ice shelf, antarctica, and the resulting impact on tributaries. *Journal of Glaciology*, **62**(235), 905–911

Schoof C (2007) Ice sheet grounding line dynamics: Steady states, stability, and hysteresis. *Journal of Geophysical Research: Earth Surface*, **112**(F3)

Schoof C (2012) Marine ice sheet stability. *Journal of Fluid Mechanics*, **698**, 62–72

Schoof C and Hewitt I (2013) Ice-sheet dynamics. *Annual Review of Fluid Mechanics*, **45**, 217–239

Seroussi H, Morlighem M, Larour E, Rignot E and Khazendar A (2014) Hydrostatic grounding line parameterization in ice sheet models. *The Cryosphere*, **8**(6), 2075–2087

Tezaur IK, Perego M, Salinger AG, Tuminaro RS and Price S (2015a) Albany/FELIX: a parallel, scalable and robust, finite element, first-order Stokes approximation ice sheet solver built for advanced analysis. *Geoscientific Model Development*, **8**, 1–24, ISSN 19919603 (doi: 10.5194/gmd-8-1-2015)

Tezaur IK, Tuminaro RS, Perego M, Salinger AG and Price SF (2015b) On the Scalability of the Albany/FELIX first-order Stokes Approximation ice Sheet Solver for Large-Scale Simulations of the Greenland and Antarctic ice Sheets. *Procedia Computer Science*, **51**, 2026–2035, ISSN 18770509 (doi: 10.1016/j.procs.2015.05.467)

Wearing M (2016) *The Flow Dynamics and Buttressing of Ice Shelves*. Ph.D. thesis, University of Cambridge

APPENDIX